

Article

Open Access



Machine learning prediction of small molecule passivators and their impacts on the passivation and photocatalytic performance of organic-inorganic hybrid perovskite interfaces

Yan Cai¹, Zhentao Bai², Changcheng Chen^{1,*}, Minghong Sun³, Zhengjun Wang¹, Songya Wang¹, Ziyi Zhang¹, Jiangzhou Xie⁴ , Dongbo Li^{1,*}, Xiaoning Guan⁵, Gang Liu⁵, Pengfei Lu⁵, Sining Yun^{6,*}

¹School of Science, Xi'an University of Architecture and Technology, Xi'an 710055, Shaanxi, China.

²School of Civil Engineering, Xi'an University of Architecture and Technology, Xi'an 710055, Shaanxi, China.

³School of Information and Software Engineering, University of Electronic Science and Technology of China, Chengdu 610054, Sichuan, China.

⁴School of Mechanical and Manufacturing Engineering, University of New South Wales, Sydney, New South Wales 2052, Australia.

⁵State Key Laboratory of Information Photonics and Optical Communications, Beijing University of Posts and Telecommunications, Beijing 100876, China.

⁶School of Materials Science and Engineering, Xi'an University of Architecture and Technology, Xi'an 710055, Shaanxi, China.

***Correspondence to:** Dr. Changcheng Chen, School of Science, Xi'an University of Architecture and Technology, No. 13, Yanta Road, Beilin District, Xi'an 710055, Shaanxi, China. E-mail: chenchangcheng@xauat.edu.cn; Dr. Dongbo Li, School of Science, Xi'an University of Architecture and Technology, No. 13, Yanta Road, Beilin District, Xi'an 710055, Shaanxi, China. E-mail: ldb@xauat.edu.cn; Dr. Sining Yun, School of Materials Science and Engineering, Xi'an University of Architecture and Technology, No. 13, Yanta Road, Beilin District, Xi'an 710055, Shaanxi, China. E-mail: yunsining@xauat.edu.cn

How to cite this article: Cai, Y.; Bai, Z.; Chen, C.; Sun, M.; Wang, Z.; Wang, S.; Zhang, Z.; Xie, J.; Li, D.; Guan, X.; Liu, G.; Lu, P.; Yun, S. Machine learning prediction of small molecule passivators and their impacts on the passivation and photocatalytic performance of organic-inorganic hybrid perovskite interfaces. *Energy Mater.* 2025, 5, 500043. <https://dx.doi.org/10.20517/energymater.2024.185>

Received: 23 Sep 2024 **First Decision:** 6 Nov 2024 **Revised:** 20 Nov 2024 **Accepted:** 2 Dec 2024 **Published:** 18 Feb 2025

Academic Editor: Meicheng Li **Copy Editor:** Fangling Lan **Production Editor:** Fangling Lan

Abstract

Organic-inorganic hybrid perovskite materials show great potential in photocatalysis and solar cells due to their excellent photoelectric properties, while interface defects affect their photocatalytic performance and stability. In this study, machine learning techniques were used to perform preliminary screening and prediction of high-performance passivation molecules (PMs), and density functional theory was used to investigate the effect of PMs on interfacial passivation performance. It was found that the presence of different chemical bonds between PMs and the interface can significantly change the interface properties. Therefore, the effect of PMs on the performance



© The Author(s) 2025. **Open Access** This article is licensed under a Creative Commons Attribution 4.0 International License (<https://creativecommons.org/licenses/by/4.0/>), which permits unrestricted use, sharing, adaptation, distribution and reproduction in any medium or format, for any purpose, even commercially, as long as you give appropriate credit to the original author(s) and the source, provide a link to the Creative Commons license, and indicate if changes were made.



of interfacial photocatalytic CO₂ reduction reaction was explored. When PMs present N-Pb bonds at the interface, CO₂ is reduced to CH₃OH, while S-Pb bonds selectively generate CH₂O from CO₂, making perovskite selectively generate O-containing carbonyl compounds. The autocatalytic performance of organic compounds at the perovskite interface is poor and is not easy to occur. This study combines perovskite interface passivation and photocatalytic performance, providing a new approach for selective catalysis at perovskite interfaces.

Keywords: Organic-inorganic hybrid perovskite, functional ligand organic small molecules, interface passivation, photocatalytic CO₂RR, machine learning

INTRODUCTION

Organic-inorganic hybrid perovskite [methylammonium lead iodide perovskite (MAPbI₃)] has demonstrated a power conversion efficiency (PCE) of 25.78% in its solar cell devices^[1]. This high performance is attributed to its excellent carrier diffusion length^[2], high defect tolerance^[3], high absorption coefficient^[4], low non-radiative recombination rate^[5], and long carrier lifetime^[6]. These excellent properties are attributed to the introduction of organic molecules, which reduce the energy barrier between bands, facilitating the occurrence of quantum tunneling effects^[7]. Therefore, it is widely applied in some fields such as photodetectors^[8], light-emitting diodes^[9], and solar cells^[10]. However, perovskite solar cells still suffer from issues such as poor long-term stability and unstable performance, which hinder their large-scale commercialization^[11,12]. This is mainly due to the polycrystalline structure that inevitably forms during the preparation process, leading to fractures at grain boundaries or surfaces, creating defects^[13]. These defects are prone to react with water and oxygen in the air to form superoxide (O²⁻)^[14]. The formation of superoxides triggers continuous photodegradation reactions and non-radiative recombination in the structure^[15]. In perovskite materials, most defects arise from the volatilization of iodine (I) atoms at the interfaces, resulting in the formation of unsaturated coordination (Pb²⁺) by lead (Pb)^[16,17]. These Pb²⁺ can react with oxygen in the air to form lead oxide (PbO). Additionally, these under-coordinated Pb²⁺ can also form lead dimers, further contributing to structural degradation^[18]. To improve the long-term stability of perovskites, defect engineering has been widely studied. Among various regulation methods, Lewis acids/bases can effectively inhibit the formation of defects, enhance structural stability, and adjust the energy level alignment between the perovskite and the transport layers, thereby improving the photovoltaic performance of the devices^[19]. The N and S atoms, which can provide lone pair electrons, have an important electron-donating role in Lewis bases. This is because the passivation of small molecules containing N and S atoms can provide lone pairs of electrons, forming coordination bonds with uncoordinated Pb²⁺ or halide anions through van der Waals forces, thereby repairing defect states and preventing further structural degradation^[11,20]. Therefore, the aromatic amine passivators containing N and S atoms play a crucial role in passivating defects and enhancing structural properties at the perovskite interface.

Secondly, many researchers have explored the ability of cocatalysts such as pyridine (Py) to enhance the selectivity of semiconductor electrodes (such as GaP, CdTe, and CuInS₂) for CO₂ reduction to methanol or formic acid^[21-24]. In this process, the electrode needs to be reduced to activate the semiconductor material, which then transfers electrons to the aromatic amine, enabling it to undergo a series of electron transfer and proton-coupled processes, thereby achieving the reduction of CO₂^[21,25]. Semiconductor reduction electrodes and perovskite systems, although composed of different components, both belong to semiconductor materials. They can both activate and reduce CO₂ through carrier activation at the interface. Moreover, it has been explored that the interaction between fullerene C₆₀ and perovskite interfaces promotes the separation of photogenerated carriers at the interface, thereby significantly enhancing the performance of the system in photocatalytic reduction of CO₂^[26,27]. Therefore, investigating the effect of aromatic amines at the perovskite interface on photocatalytic CO₂ reduction is feasible. Among various perovskite materials,

MAPbI₃ has been selected as a novel photocatalytic semiconductor material due to its excellent absorption of visible light^[28]. Based on this, this paper innovatively explores the role of aromatic amines at the interface of MAPbI₃, investigating their impact on the selective photocatalytic reduction of CO₂ at the interface.

However, using traditional experimental and theoretical research methods to screen for efficient passivation materials consumes a large amount of manpower and resources, which not only reduces efficiency but also wastes a great deal of time and effort. Currently, many researchers have begun to utilize machine learning techniques to screen reliable molecules from numerous materials, reveal potential correlations between molecular characteristics, and predict unknown outcomes^[29]. Furthermore, in applying machine learning, it is necessary to establish an appropriate mapping relationship between the feature vectors of small molecule passivators and the output variables. To achieve better predictive performance for passivation, we need to select suitable algorithms from a variety of machine learning models, including Random Forest (RF), Artificial Neural Networks (ANN), Support Vector Regression (SVR), and Linear Regression (LR). This study established the relationship between the output variable ΔPCE and the independent variables [dipole moment (DM), exact mass (EM), and isotopic mass number (MM)] using a machine learning algorithm. Many researchers have explored the use of machine learning models to identify potential organic passivating agents that can enhance the performance of MAPbI₃ photovoltaic devices^[30-32]. For example, Zhi *et al.* utilized machine learning to select the optimal organic cations for passivating MAPbI₃ perovskite solar cells^[30]. They established a relationship between molecular features (such as complexity, molecular weight, O atoms, and so on) and output *PCE*. The prediction of the 5-carboxyphthalocyanine (5-CP) additive enhancing device *PCE* was confirmed through density functional theory (DFT) calculations and experimental exploration. Machine learning can effectively predict small molecule passivators with excellent passivation performance, providing a subject for the in-depth study of the interactions between small molecule passivators and interfacial photocatalytic performance.

In this study, we first screened and predicted high-performance Py analog small molecule passivators using machine learning. Subsequently, DFT calculation and device simulation were used to verify the passivation effect between passivation molecules (PMs) and MAPbI₃ interfaces. The results show that in the same passivating molecule, different functional groups and interfacial bonding modes have significant effects on the passivation performance. For example, the synergy between N-Pb and SH...I chemical bonds can improve the interface energy level alignment, reduce the charge accumulation at the interface, and enhance the device *PCE*. However, the S-Pb bonding leads to more torsion of the perovskite octahedra, which reduces the structural *PCE*. Different chemical bonding modes can significantly change the interfacial properties. Therefore, the effect of PMs on the interfacial photocatalytic CO₂ reduction reaction (CO₂RR) was further explored. The results show that when CO₂ is adsorbed at the MAPbI₃ interface containing passivator molecules, the N-Pb bond in PMs will make the adsorption site of CO₂ move to the opposite side of PMs, which is due to the vertical adsorption effect of SH...I coordination bonds. At the same time, the larger hole site below the C-S covalent bond makes the CO₂ more distant from the PMs, resulting in the selective reduction of CO₂ to CH₃OH. On the other hand, the S-Pb bond favors the adsorption of CO₂ on PMs. The N atom has strong electronegativity, which forms a negative electric field around it. Upon adsorbing CO₂, it interacts with the molecule and forms a non-covalent bond σ -hole effect, which promotes the selective reduction of CO₂ to OCH₂ at the interface. This study reveals the theoretical mechanism of PMs acting on the perovskite interface to selectively photoreduce CO₂ to oxygen-containing carbon-based compounds.

COMPUTATIONAL METHODS

Machine learning

The machine learning process in development and simulation requires four key steps, and this model focuses on selecting effective passivation molecules from a broad molecular library for solar cells, as shown in Figure 1A and Supplementary Figure 1A. Firstly, the initial stage involves constructing a rich dataset of passivation small molecules. This dataset includes information and feature vectors that characterize the small molecules. Based on existing literature and reported datasets, we have created a database of small molecules used for passivation. Secondly, relevant feature variables are identified to describe changes in passivation performance. In addition, the Pearson correlation method is applied to analyze the dataset, with the aim of eliminating redundant features that are statistically similar to other features. Subsequently, various algorithms are employed to build machine learning models, which are trained based on the dataset constructed in the first step. Finally, models are evaluated using data screened on a large scale through methods such as RF and Neural Networks, with the goal of minimizing evaluation bias. Given the small size of the passivated molecule dataset, it is necessary to introduce new evaluation methods to improve model accuracy. Here, we utilize the commonly used cross-validation method to investigate the effective passivation performance of passivated molecules and test the dataset.

Among them, the dataset is crucial to machine learning. We have collected relevant literature published between 2018 and 2023 on small molecule passivants acting on the surface of perovskites, integrating approximately 200 data [Supplementary Material Database]. The regression model links 26 specific molecular features to the PCE improvement ratio^[30]. Smaller datasets can lead to overfitting phenomena, so we used SHapley Additive Explanations (SHAP) analysis to identify the most important molecular features^[33]. The number of representative features is further effectively reduced to five. This is used to reveal how molecular characteristics influence passivation performance^[34]. In order to predict the characteristics, four machine learning regression models - RF^[35], SVR^[36], K-Nearest Neighbors (KNN)^[37] and Gradient Boosting (GB)^[38] Regressor - were used to find the optimal mapping between features and target features. This was followed by selecting one suitable candidate material for predicting passivation performance to validate the feasibility of machine learning screening.

Density functional theory

Based on DFT, first-principles calculations were performed using the Vienna Ab initio Simulation Package (VASP)^[39]. The electronic exchange-correlation function was handled using the Perdew-Burke-Ernzerhof (PBE) method of the generalized gradient approximation (GGA) and computed with the projector-augmented wave (PAW) method^[40,41]. The cutoff energy was set to 400 eV, and the *k*-point mesh in the Brillouin zone was $2 \times 2 \times 1$. The convergence thresholds for relaxation forces on each atom and ion, and for self-consistent energy, were 0.01 eV/Å and 1×10^{-5} eV, respectively^[42-44]. A vacuum region of 15 Å was introduced to prevent periodic interactions, and the van der Waals interactions between layers were considered and corrected using DFT-D3^[45,46]. Determine charge transfer characteristics through analysis of Bard charges. Calculations were performed on the full band structure, partial density of states (PDOS), and bandgaps along several high-symmetry directions. In this work, the valence electron structure of the atom is H $1s^1$, C $2s^2 2p^2$, N $2s^2 2p^3$, S $3s^2 3p^4$, Pb $5d^{10} 6s^2 6p^2$, I $5s^2 5p^5$. All calculations were performed on the PbI₂-terminated surface of the MAPbI₃(001) surface, where Zuo *et al.* revealed that Pb acts as the adsorption activation site for the CO₂RR^[45]. The bonding and anti-bonding distributions between reactants were analyzed using the projected crystalline orbital Hamiltonian population (pCOHP). Supplementary Table 1 provides the possible pathways and corresponding minimum energies required for the CO₂ reduction process. For more details, please refer to the Supplementary Material.

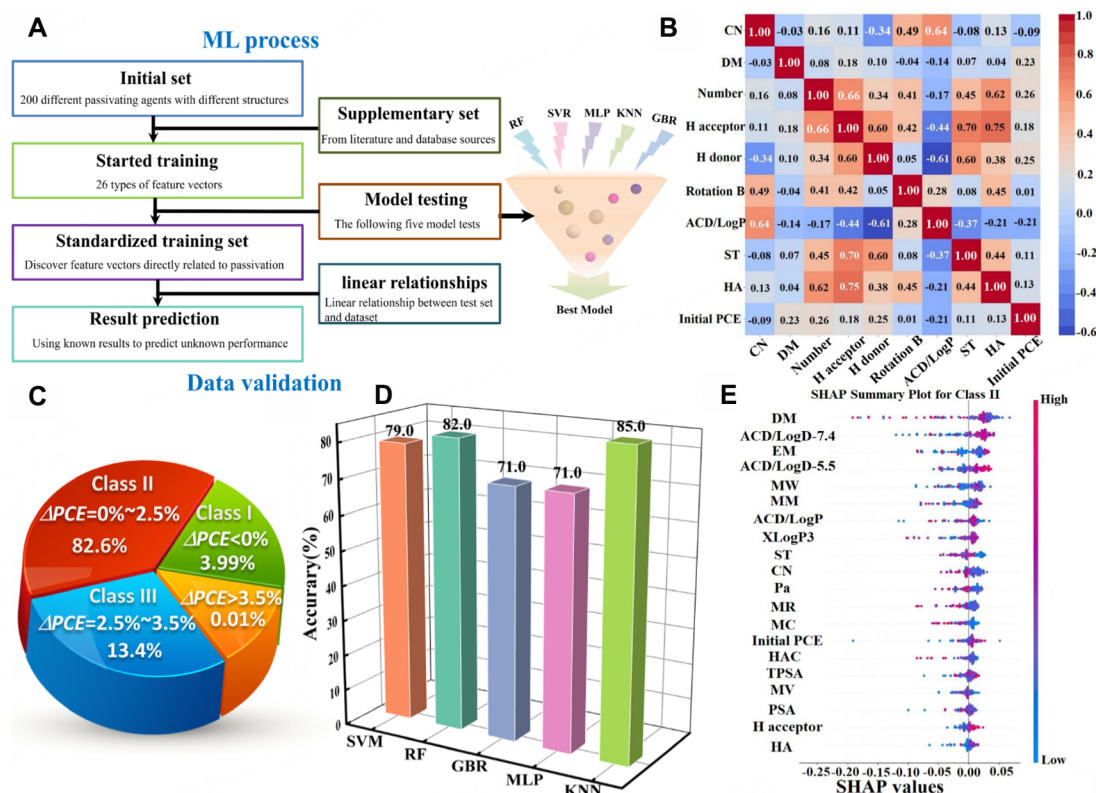


Figure 1. (A) The calculation process of ML. (B) Correlation matrix of Pearson coefficients for the ten selected feature descriptors, where positive and negative values indicate positive and negative correlations, and numeric values represent the degree of correlation. (C) Proportional classification of the ΔPCE data. (D) Accuracy calculated by a single ML model. (E) Ranking of the importance of different eigenvectors in type II. The SHAP value represents a positive or negative contribution to the efficiency of the device. Red corresponds to high-value features, while blue corresponds to low-value features.

Device simulation

In this study, the current density-voltage (J - V) plots, open-circuit voltage (V_{oc}), short-circuit current (J_{sc}), fill factor (FF), and PCE of Au/TiO₂/MAPbI₃/PMs/2,2',7,7'-Tetrakis[N, N-di(4-methoxyphenyl)amino]-9,9'-spirobifluorene (Spiro-OMeTAD)/fluorine-doped tin oxide (FTO)^[47] solar cells with MAPbI₃ as the absorber were calculated using the numerical simulation program One-Dimensional Solar Cell Capacitance Simulator (SCAPS-1D)^[48,49]. The same method was used to study the changes of PCE before and after passivation. **Supplementary Figure 1B** shows the basic structure of n-i-p PSC considered in the study, with TiO₂ as electron transport layer (ETL) and Spiro-OMeTAD as hole transport layer (HTL). Device simulations were performed on the material based on known relevant data, and specific parameter settings can be found in **Supplementary Table 2**.

RESULTS AND DISCUSSION

The screening process of machine learning

We evaluate passivation performance using the change in PCE before and after passivation, with the corresponding output as PCE and the input variables being the molecular chemistry of the device (e.g., polarization, molecular complexity, etc.) and the original PCE . To handle various data schemas, we employ different machine learning models such as Support Vector Machine (SVM), RF, and eXtreme Gradient Boosting (XGB), which helps reduce the likelihood of overfitting in small training datasets. Using too many feature descriptors in a limited dataset can lead to overfitting, so it is necessary to select important

descriptors to represent ΔPCE . The Pearson correlation coefficient is a statistical metric that describes the degree of linear correlation between two variables, denoted by $|p|$ ^[50]. The number of feature vectors was reduced from 26 to 10 with the relevant guidelines (specific guidelines can be found in the [Supplementary Material](#)). [Figure 1B](#) shows the Pearson correlation matrix, which visually illustrates the relationships between feature vectors. We first created the corresponding regression model using four models, XGB, RF, GB, and SVR [[Supplementary Figure 1C-F](#)], and evaluated the accuracy of the model using the coefficient of determination (R^2). The closer the R^2 value is to 1, the more reliable the predictive model will be. Using the regression model, we found that the R^2 of all predictive models was very small [[Supplementary Figure 2A](#)], suggesting that the regression model is not suitable to describe the small molecule passivation performance of the perovskite devices in our database. Based on this, we also use a stacked model for further predictions, as shown in [Supplementary Figure 2B](#). Although R^2 shows significant improvements, it also leads to data fouling and overfitting. Subsequently, we created a classification model for prediction. A classification model refers to the assignment of data features, the creation of a model, and the use of the model to predict new data, which has better predictive power than a regression model^[51].

The ΔPCE datasets were divided into four categories: $\Delta PCE < 0\%$ Class I, $\Delta PCE: 0\% \sim 2.5\%$ Class II, $\Delta PCE: 2.5\% \sim 3.5\%$ Class III, and $\Delta PCE > 3.5\%$ Class IV [[Figure 1C](#)]. However, due to the limited number of Class IV samples, they were excluded from the simulation, and the study focused on three categories for evaluation of the five models [[Figure 1D](#)]. Under a single algorithm, the highest accuracy of KNN is 85%, and here we set the K value to 10. In order to quantify the contribution of each X to Y, we use SHAP additive interpretation to reflect the influence of feature vectors on the results. The magnitude of the SHAP value indicates the importance of the input variable to Y, with a positive or negative value reflecting whether the X eigenvalue is positively or negatively correlated with the SHAP value. In Class II, the SHAP values contribute the most to the model's predictions, so most of the systems we study fall into this category. The DM, ACD/LogD-7.4, EM, and ACD/LogD-5.5 all have a significant impact on the output variable Y. For the value of the remaining SHAP types, see [Supplementary Figure 2C](#) and [D](#). Here, DM, ACD/LogD-7.4, EM and ACD/LogD-5.5 are all positively correlated with SHAP values, as shown in [Figure 1E](#).

Research on passivation performance

Structural features

By exploring the relationship between feature vectors in machine learning and SHAP, we understand the relationship between feature vectors in passivators and PCE . In order to further investigate the effect of PMs on interfacial catalytic performance, we selected 2-mercaptopyrimidine (2-Mpym) and its analogs as candidate small molecules for prediction. Although Zang *et al.* reported that 2-Mpym can forcefully passivate at the MAPbI₃ interface, reduce the density of states of surface defects, enhance device stability, and further improve the structure PCE , the bonding mode, morphology and further theoretical studies of 2-Mpym and its analogs and interfaces have not been reported^[52]. Furthermore, compounds such as 2-Mpym analogs, including Pyrimidine-5-thiol (5-Py) and 2-mercaptopyrazine (2-Py), have yet to be deeply explored for their effects on the perovskite interface.

Firstly, we calculated that the 2-Mpym has different bonding patterns with the interface, with 2-Mpym(N) for N-Pb bonding and 2-Mpym(S) for Pb-S bonding. Different bonding methods of PMs can alter the performance of the interface, resulting in different results for interface passivation. Similar extended studies were conducted on the passivation effect of 2-Mpym and its derivative 4-mercaptopyridine (4-Mpy), as well as the influence of different N sites, 5-Py and 2-Py, in 2-Mpym on passivation performance. As shown in [Supplementary Figure 3](#) and [Figure 2A](#), the crystal lattice undergoes varying degrees of distortion after adsorption of the small molecule passivator, but there is no significant change in the lattice constant [[Supplementary Table 3](#)], indicating that the small molecule passivator exhibits a strong interaction with the

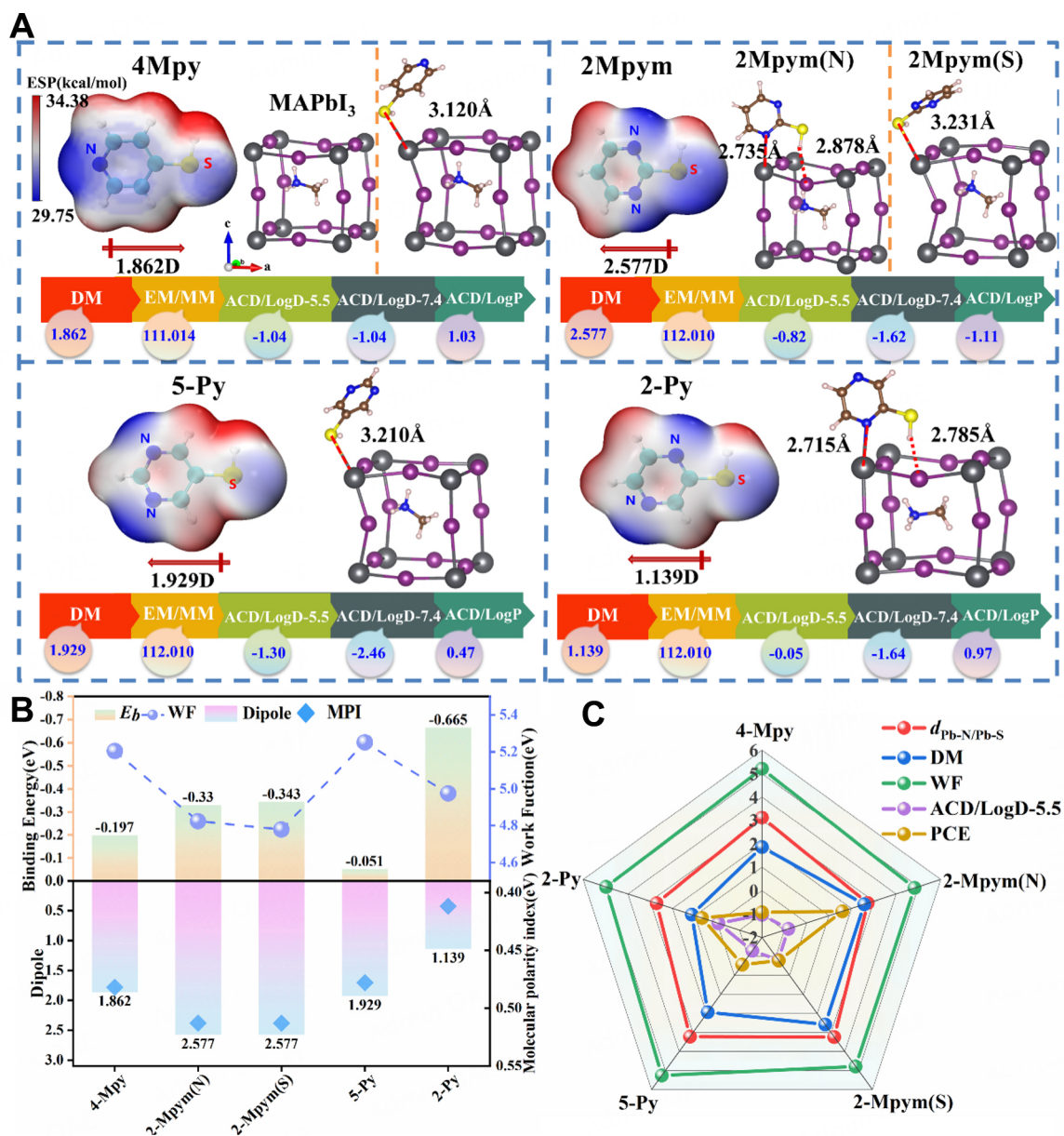


Figure 2. (A) The electrostatic potential of passivating agent molecules, along with the geometric model and bond lengths before and after adsorption. The dark gray, blue, yellow, purple, and white spheres represent Pb, N, S, I, and H atoms, respectively. The arrow indicating the electric dipole moment shows the direction of the dipole projection. The color annotation card represents the top five important feature vectors, with the following values providing their respective sizes. (B) The relationship diagram between the binding energy E_b , surface work function (WF), dipole moment, and corresponding molecular polarity (MPI) after passivation with different PMs. (C) Radar diagram of the relationship between key length $d_{\text{Pb-N/Pb-S}}$, DM, WF, ACD/LogD-5.5, and Z-score normalized PCE.

surface, and this strong interfacial interaction leads to a new arrangement of the electron cloud within the lattice, resulting in defective impurity energy levels to adjust the bandgap and alter the electronic and optical properties of the structure. The calculated binding energies (E_b) are all negative, indicating that this lattice distortion is within the structural stability range. Furthermore, when I-H hydrogen bonds appear on the surface, small molecule passivators are vertically adsorbed on the surface, while other passivators are adsorbed on the lattice surface at an angle. The extended S-H hydrogen bonds can be bonded to nearby I atoms to form I-H bonds, and the adsorption of multiple bond energies can promote structural stability. In

addition, ab initio molecular dynamics simulations (AIMD) are calculated to evaluate the stability of the interface. Here, we calculated the AIMD of different PMs acting on the perovskite interface. The Nose Hoover temperature control method is used to set the temperature to 300 K, the time step to 2fs, and the number of steps to 3,000, as shown in [Supplementary Figure 4](#). The results show that the PMs reach energy equilibrium after 1,000 fs and oscillate near the equilibrium value, indicating that the studied PMs acting on the perovskite interface are thermodynamically stable. All Pb-N bonds have distances between 2.7–3.3 Å, which is shorter than the length of the Pb-S bond. Therefore, the molecule is more likely to form a Pb-N adsorption type. As can be seen from [Figure 2B](#), 2-Py with smaller DM has lower E_b , indicating that the structure is more stable. Conversely, 5-Py with a high DM produces a higher E_b . The work function (WF) is used to determine the transport capacity of electron hole pairs to the surface of the structure^[53].

As shown in [Figure 2B](#) and [Supplementary Table 3](#), the value of WF can be obtained, confirming that PMs with more surface chemical bonds have lower E_b , and lower WF. The 2-Mpym(N) and 2-Py can facilitate carrier transport. [Figure 2C](#) shows the radar relationship among $d_{\text{Pb-N/Pb-S}}$, DM, WF, ACD/LogD-5.5, and Z-score normalized PCE, respectively. It can be observed that the 2-Mpym(N) has the largest PCE and the corresponding DM is larger, while WF, $d_{\text{Pb-N}}$, and ACD/LogD-5.5 are smaller. However, 2-Py has a relatively small DM, but ACD/LogD-5.5 is relatively large, and it has a minor larger PCE. This is consistent with the predictions of machine learning.

Electronic optical performance

According to the band diagram (Band) and projected density of states (PDOS), it is observed that the valence band (VB) of the intrinsic structure MAPbI₃ is mainly composed of hybridization between Pb 6s orbitals and I 5p orbitals, producing a σ^* anti-bonding state, in which I 5p orbital makes the largest contribution, while conduction band (CB) mainly comprises Pb 6p orbitals, as shown in [Figure 3A](#). The organic cation MA primarily acts as a charge compensation center and contributes little to the band edge. The intrinsic structure has a bandgap of 1.829 eV, which is similar to the 1.79 eV bandgap reported by Filip et al.^[54]. [Supplementary Figure 5A](#) and [B](#) can directly see the σ^* anti-bonding state between I p and Pb s orbitals, and the coupling state between I p and Pb p orbitals, which confirms the above discussion. Combined with the passivated PDOS [[Figure 3B–F](#)], it can be seen that PMs contribute little to the bandgap and only have an effect on the deep energy level. The CB in the eigensystem mainly comes from the highly hybrid states of p_x and p_y in Pb 6p orbitals, and the p_x orbit contributes the most in the I 5p orbitals, as shown in [Figure 3G](#). The molecular orbital (MO) model and PDOS diagram of each PM are shown in [Figure 3H–L](#), where the lowest unoccupied molecular orbital (LUMO) anti-bonding π^* orbital of PMs is formed by the coupling of N 2p and C 2p orbitals, and S 2p orbitals contribute more to the formation of highest occupied molecular orbitals (HOMO). After 2-Mpym(N) and 2-Py passivation, the bandgap is obviously reduced, and electrons are easily transferred to the electrode through CB. However, the weaker the electronegativity of S atoms in 2-Mpym(S), the higher the HOMO energy, resulting in the distortion of the interface structure, the energy level away from conduction band minimum (CBM), and the increase of the bandgap. The difference brought about by 2-Mpym is that the strong electron acceptor N atom forms a better coordination bond with Pb²⁺, thereby reducing the bandgap. On the contrary, after passivation with 4-Mpy and 5-Py, due to the energy level mismatch with Pb at the interface, the interface Pb-I-Pb collapses downward, resulting in the generation of defect states and the increase of bandgaps. A larger bandgap will inhibit electron-hole recombination, thereby increasing V_{OC} .

Bonding state

In PM MOs [[Figure 4A](#)], π_1 , π_2 , and π_3 are bonding orbitals, and π_1^* , π_2^* are anti-bonding orbitals, where π_1 and π_2 are degenerate. The π_2^* orbital pattern, with all adjacent phases being the same, forms a cyclic large π

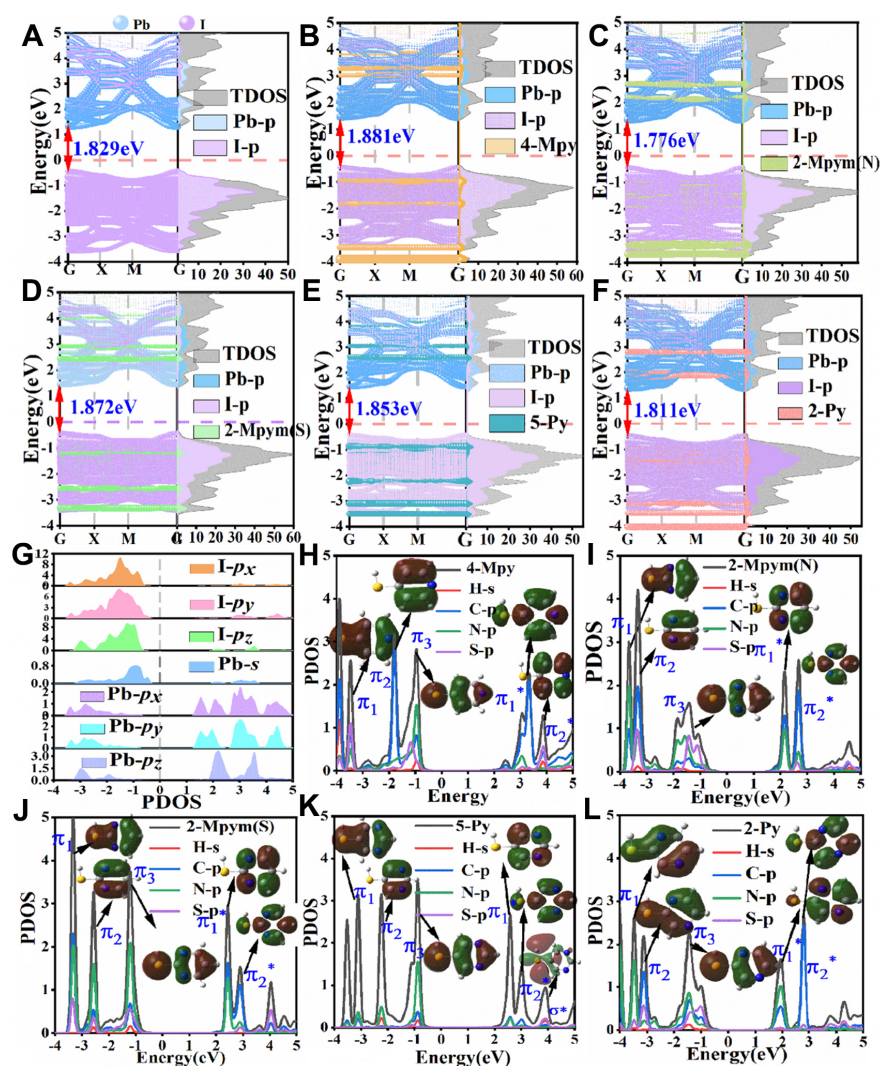


Figure 3. (A-F) are the energy bands (Band) and total density of states (TDOS) for the intrinsic structure and adsorption of different PMs, respectively. The Fermi level is set to 0. (G) In the intrinsic structure, the partial density of states (PDOS) of the I atom and the Pb atom. (H-L) are the relevant orbitals and orbital diagrams corresponding to the partial and total density of states of small molecule passivators, respectively.

bond, forming a single ring planar conjugated system, and its π electron number is 6, satisfying the Hückel rule^[55]. It has aromaticity and is prone to electrophilic substitution reactions on the ring, which can promote structural stability. The atom of PMs is a π cyclic conjugated system, with the highest occupied orbital exhibiting obvious anti-bonding π^* orbital characteristics and nucleophilic ability. Electrons on the anti-bonding π^* orbital can act as electron donors to interact with the Pb^{2+} ions on the surface and transfer to the surface. When PMs bond with Pb atoms, electrons jump from the CBE of MAPbI_3 to the LUMO orbitals of PMs [Figure 4B], thereby improving the interface energy level arrangement. Supplementary Table 4 gives the energy levels and bandgap values between PMs, and it is known that 2-Mpym(N) and 2-Py have small gaps to promote electron transport, which is consistent with the theory found by machine learning. Good energy level matching can generate a larger built-in electric field at the interface, promoting unidirectional charge transport.

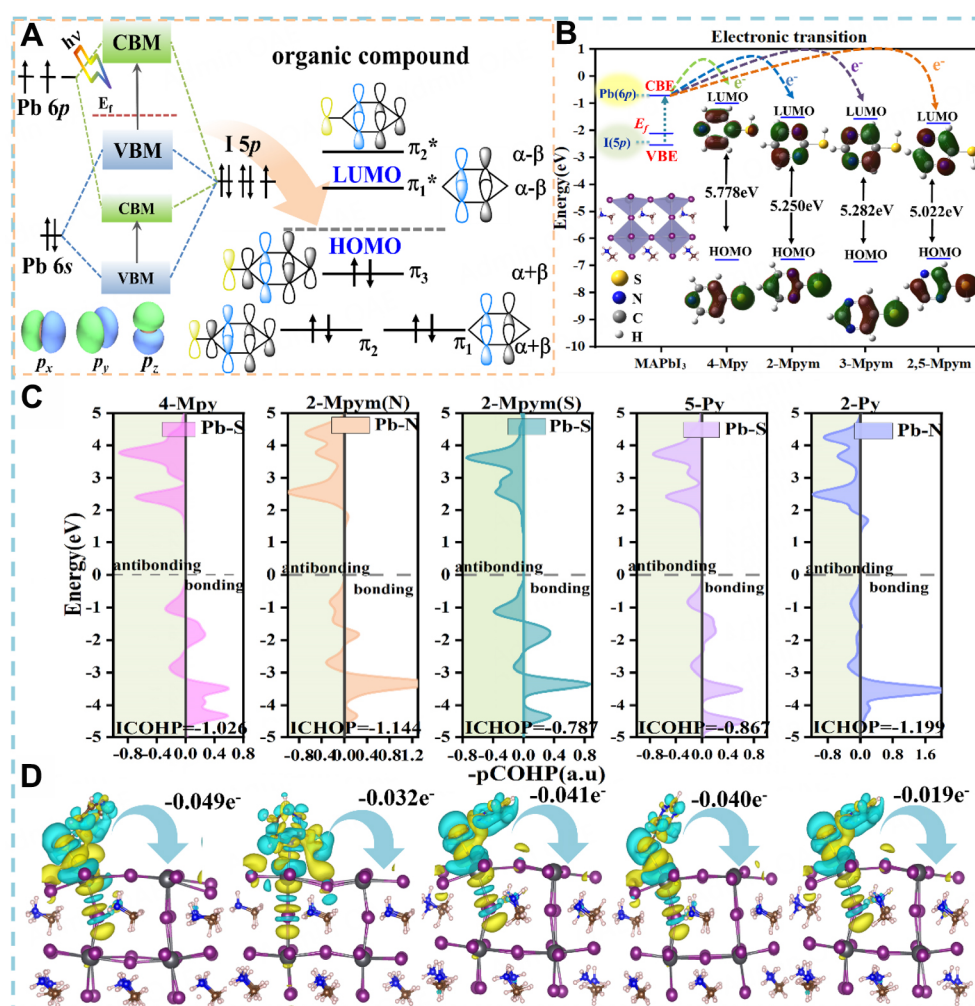


Figure 4. (A) Transition model and orbital diagram between interfaces and PMs. (B) Energy level relationship between the CBM, VBM on the MAPbI₃ interface and LUMO, HOMO in PMs. (C) The pCOHP diagrams of Pb-S or Pb-N bonds after passivation with different PMs. (D) presents the differential charge (CDD) plots of 4-Mpy, 2-Mpym(N), 2-Mpym(S), 5-Py, and 2-Py after passivation were obtained. The yellow part represents the area of charge accumulate S ion, while the blue part represents the area of charge depletion.

In order to gain a deeper understanding of the bonding state of the adsorption system, we conducted projection COHP (pCOHP) analysis on the S-Pb or N-Pb bonds [Figure 4C]. The COHP projects band structure energy into orbital pair interactions and can provide relative contributions of bonding, nonbonding, and anti-bonding states for a given bond as a function of energy^[56]. For all adsorbed PMs, the anti-bonding states of S-Pb or N-Pb are very close to E_F indicating that anti-bonding orbitals dominate. The integrated COHP (ICOHP) value indicates that the N-Pb bond has a more negative anti-bonding state, indicating a higher degree of N-Pb bond activity after passivation with 2-Mpym(N) and 2-Py. According to the MO theory, the outermost electrons are the first to participate in the bonding process, and the Pb 6p² orbital is the first to undergo P-P orbital hybridization with the S 3p⁴ or N 2p⁴ orbital to form a σ^*/π^* anti-bond. Among them, the Pb-N/Pb-S bonds of 4-Mpy, 2MPym(N), 2MPym(S), and 5-Py all exhibit σ^* bonds, while the Pb-N bonds of 2-Py exhibit π^* bonds. At the same time, S 3p⁴ or N 2p⁴ also participates in the coupling process of PMs conjugated orbitals. The hybridization state diagram is shown in Supplementary Figure 5C-G. Using electron localization function (ELF) to study the bonding characteristics at the interface, as shown in Supplementary Figure 5H, it can be seen that S-Pb and N-Pb exhibit ionic

valence bonds. Additionally, S and N have lone pair electrons, making the molecule more nucleophilic and able to form ionic bonds with Pb^{2+} . Furthermore, strong ionic bonds can better stabilize under coordinated Pb and prevent the formation of Pb-Pb dimers^[18].

The differential charge (CDD) in Figure 4D and Bader charge transfer data in Supplementary Table 5 show that the gain and loss of charge are both near the PM interface, and electrons undergo rearrangement. After passivation, all charges are transferred from PMs to the surface of perovskite, while the Pb atom loses about 0.504–0.902 e^- , and the I atom gains electrons, which is beneficial for charge transfer and hole extraction at the MAPbI_3 /PMs/hole transport material (HTM) interface. The uneven distribution of the electric field results in a huge internal electric field (IEF) generated at the interface from perovskite to PMs, which facilitates the transport and separation of photogenerated electron-hole pairs^[57], and can alter the photocatalytic ability of the interface. The molecules that form S-Pb ionic bonds at the interface can transfer more electrons at the interface, causing a larger deviation angle of PMs. The predominance of anti-bonding orbitals at the interface is detrimental to structural stability. PMs belonging to aromatic hydrocarbons have conjugated π -cyclic systems that can promote charge migration to improve interface energy level alignment, reduce charge accumulation at the interface, and enhance device PCE.

Perovskite PMs@MAPbI₃ device simulation of solar cell device SCAPS-1D

To better describe PMs@MAPbI₃, we investigated the passivation performance in an n-i-p structured perovskite solar cell with a configuration of FTO/Spiro-OMeTAD/PMs@MAPbI₃/TiO₂/Au, as shown in Figure 5A. This structure is illuminated under an AM 1.5G solar spectrum with an incident power density of 100 mW cm^{-2} . Due to the strong ionic bonding of N-Pb and the formation of stable IEF at the interface, passivation with 2-Mpym(N) and 2-Py can improve the PCE of the device, increase the V_{OC} , reduce the J_{SC} , and achieve passivation performance, as shown in Figure 5B. The device PCE is closely related to the structural bandgap of *p*-type semiconductors PMs@MAPbI₃. In addition, the passivation with 2-Mpym(N) and 2-Py results in an ideal bandgap for perovskite devices, making it easier for electrons to transition to CBM and generate excitons, as shown in Figure 5A. At a wavelength of around 300nm, the monochromatic photon electron conversion efficiency (IPCE) of the intrinsic structure is higher, while around 700 nm, both 2-Mpym(N)@MAPbI₃ and 2-Py@MAPbI₃ exhibit excellent IPCE performance. It can be observed that the photoelectric conversion wavelength of 2-Mpym(N) and 2-Py has experienced a redshift, as shown in Figure 5C. We found that the 2-Mpym(N) and 2-Py systems can promote an increase in PCE by 1.17% and 0.24%, respectively, belonging to Class II. The improvements in DM and PCE are positively correlated, while EM and ACD/LogD-7.4 are negatively correlated with PCE. Additionally, 4-MPy, 2-MPym(S), and 5-Py, which belong to Class I, reduced the increase in PCE by -1.41%, -1.26%, and -1.04%, respectively. The increase in DM and PCE showed an inverse correlation, confirming the machine learning model theory. However, it is important to note that although machine learning models can effectively screen and predict high-performance PMs, the predictions of these models may be limited by specific data sets and application scenarios. For example, under different experimental conditions or with varying types of perovskite materials, the validity of some predicted results may decrease.

Effect of molecule passivators on photocatalytic performance

Perovskite halides also exhibit excellent catalytic performance. The ability of photocatalysts to match the thermodynamic threshold of chemical reactions depends on the potential of their bandgaps, the minimum CB value, and the maximum VB value. The photocatalytic reduction reaction can only occur when the bandgap of the material meets certain conditions for the recombination of VB and CB edge potentials. For MAPbI₃ and PMs@MAPbI₃, the band edge potential of the VB and CB is defined as follows^[58,59]:

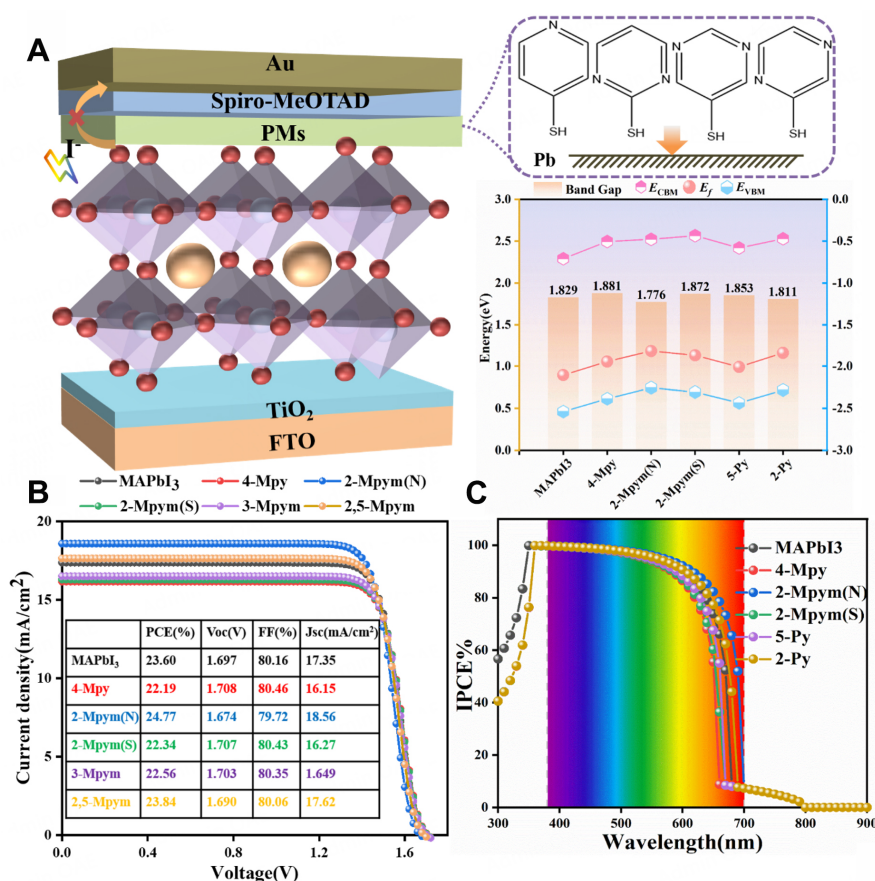


Figure 5. (A) Schematic diagram of n-i-p perovskite device structure. The Fermi energy E_F , the highest occupied orbital energy E_{CBM} , the lowest unoccupied orbital energy E_{VBM} and bandgap E_g value of the PMs@MAPbI₃. Comparison of (B) J-V curves and (C) quantum efficiency of devices with different absorption layers.

$$E_{VB} = \chi - E_e + 0.5E_g \quad (1)$$

$$E_{CB} = E_{VB} - E_g \quad (2)$$

where E_e is the energy of free electrons on the hydrogen scale [4.5 eV vs. normal hydrogen electrode (NHE)], χ is the average electronegativity of the molecules, and E_g refers to the energy band.

The band edge potential calculated using Millikan approximation is shown in Figure 6A, and all materials have the ability to generate CH₄ from CO₂. However, in the final calculation, we found that only MAPbI₃ can convert CO₂ into CH₄. Adding materials with different PMs can lead to varying degrees of collapse in the quantum effects on the surface of the structure, resulting in changes in the interface potential barrier and the production of different products, giving the structure selective catalytic performance. In subsequent exploration, we found that 4-Mpy, 2-Mpym(S), and 5-Py, when adsorbed on MAPbI₃, can selectively reduce CO₂ to formaldehyde (OCH₂); when 2-Mpym(N) and 2-Py are applied at the interface, CO₂ can be selectively reduced to methanol (CH₃OH) in Supplementary Figure 6A. According to the d-band theory, the anti-bonding coupling filling state plays a crucial role in catalytic active sites^[60]. This state can be evaluated by analyzing the Hamiltonian population (COHP) of Pb-O bond orbitals after CO₂ adsorption at the interface, as shown in Figure 6B.

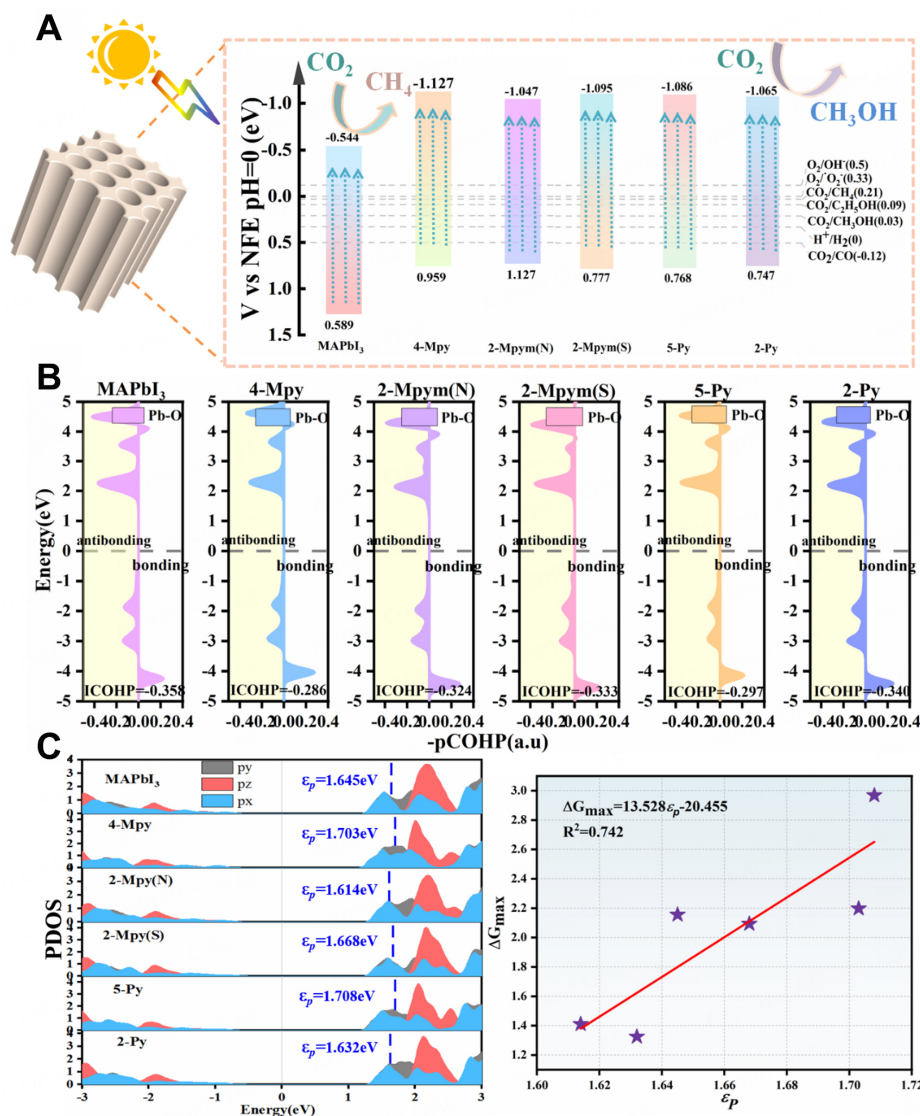


Figure 6. (A) Schematic diagram of edge potential for intrinsic structures and PMs@MAPbI₃. (B) The pCHOP of Pb-O bonds at the interface after CO₂ adsorption. (C) The left and right figures respectively show the partial density of states (PDOS) of Pb 6p orbitals after CO₂ adsorption and the linear relationship between the *p*-band neutrality (ϵ_p) of Pb atom and G_{max} . (The center of the *p*-band is indicated in blue font).

The small absolute value of ICOHP indicates that the interaction is weak, and the adsorption of different PMs weakens the adsorption performance of CO₂ at the interface to distinct degrees. This means that changes in surface charge can alter the filling of anti-bonding states, thereby affecting the kinetics of interface Pb-O bond cleavage and promoting the selective reduction ability of CO₂. Secondly, strong and weak adsorption are not conducive to the adsorption and dissociation of CO₂ at the interface for the next reaction, where 2-Mpym(N), 2-Mpym(S), and 2-Py have moderate ICOHP values. The mild and weak interaction between Pb-O is conducive to the further adsorption of proton H⁺ by CO₂ for subsequent chain reactions. The physical and chemical properties of catalysts can be characterized by their own descriptors, such as the *p*-band center (ϵ_p) of non-metallic elements and the *d*-band center (ϵ_d) of metals. These descriptors, along with their energy relative to the Fermi level (E_f) of the photocatalyst, describe the important properties of perovskite photocatalysts. For example, they can indicate the migration energy and

the excitation binding energy (E_d) of intermediates in oxidation-reduction or evolution reactions^[61,62]. By analyzing the ε_p of Pb and I atoms after CO₂ adsorption, it is found that the ε_p of Pb in 2-Mpym(N) and 2-Py is closer to the E_p while the ε_p of I is further away from E_p resulting in the decrease of ΔG_{max} [Figure 6C, Supplementary Figure 6B]. At the same time, the relationship between ε_p and ΔG_{max} can be used as a descriptor to evaluate the performance of photocatalytic CO₂. Studies have shown that adding Py or thiophene molecular catalysts to electrolytes can selectively generate alcohols or other higher-value hydrocarbons^[63]. Our exploration corresponds to this by adding pyrimidine-related organic compounds to MAPbI₃, which not only stabilizes the device from damage but also promotes the generation of interfacial alcohols and their hydrocarbon aldehydes.

The activation of the C-H bond (sp^3) plays an indispensable role in the direct conversion of hydrocarbons into high-value-added products in organic synthesis^[45]. PMs have an impact on the deep level energy levels of the structure, so the VB in the PMs@MAPbI₃ structure is mainly caused by the σ^* bond due to the hybridization of the sp orbitals. When CO₂ is coupled to the interface, the σ^* bond transfers electrons to the $2\pi_u^*$ orbital, thus activating CO₂ [Figure 7A]. According to the differential charge data (specific values from Supplementary Table 6), it can be observed that the average O atom in CO₂ loses electrons, while the C atom gains electrons. In short, the average CO₂ production rate in the PMs@MAPbI₃ system is 0.4 e⁻, which confirms the activation and reduction of CO₂ [Figure 7B].

In the PDOS diagram after CO₂ adsorption, it can be seen that the π_1^* of 2-Mpym(N) and 2-Py in CBM are closer to the Pb $6p$ orbit [Figure 8A]. In CO₂, a significant overlap between $1\pi_g$ and PMs indicates both electronic transitions and interactions between them. With the electrostatic potential diagram [Figure 8B], we can better distinguish between polarized and non-covalent σ -hole bonds formed at the interface due to electronegativity between atoms.

Compared with the original structure, the Pb-O bond length in the PMs-containing system showed different degrees of increase after CO₂ adsorption [Supplementary Figures 7 and 8], indicating that the adsorption of O atoms at the interface was enhanced. This enhancement results in the selective formation of oxygen-containing carbon-based products from CO₂. When PMs-containing Pb-N and H-I bonds interact with the interface, the CO₂ adsorption position will shift from one end of the Pb-N bond to the other. Conversely, if a Pb-S bond forms on the interface, CO₂ tends to adsorb near it. This is because S-Pb bonds facilitate interaction between the O atom and the head of the organic small molecule, causing the O atom to gain electrons and become negatively charged. As a result, a polarized bond forms at the adsorption interface. Additionally, the lone pair of electrons between N and O atoms readily form a polarized covalent bond, thus promoting CO₂ adsorption on PMs. It should be emphasized here that after CO₂ adsorption at the 2-Mpym(S) interface, the head C-H bond obtains electrons from the O atom, forming a non-covalent σ -hole bond [Figure 8B]. This weak interaction leads to sp^2 hybridization of electron-deficient carbon atom systems, and the charged molecule O atom approaches the σ -hole bond, which promotes the bias of CO₂ to PMs and enhances the adsorption of O at the interface. On the other hand, the formation of N-Pb and S-H bonds at the interface makes the interface structure more stable. The O atom at the top is not easy to have functional group contact reaction, while the O and S at the bottom form larger pore sites, so that CO₂ can be separated from the PMs. This difference leads to the selective reduction from carbon dioxide to other high-value oxygenated hydrocarbons, with structural models such as that shown in Figure 9A.

Many researchers have explored that adding organic functional groups to the surface of metals or semiconductors can reorganize interface energy levels, adjust charge transfer kinetics, and form an IEF at the interface to promote carrier transport and optimize interface catalytic ability^[64]. Through Bader charge

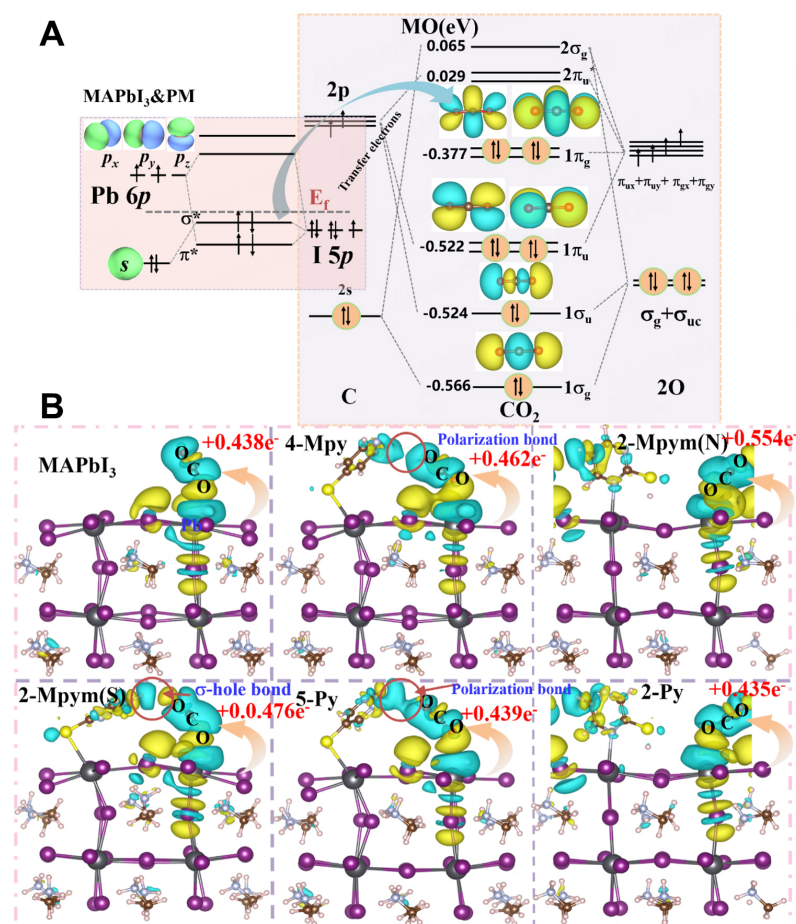


Figure 7. (A) The energy level arrangement of CO₂ and PMs indicates the transition model after interface adsorption of CO₂. (B) Differential charge and charge transfer after CO₂ adsorption. The yellow and cyan regions represent charge accumulation and consumption, respectively.

calculation, we get the results for the charge transfer of Pb^{2+} , I^- , and $^*\text{CO}_2$ in the PMs@MAPbI_3 [Figure 9B and Supplementary Table 6]. The change in charge of PMs before and after CO_2 adsorption is PMs, while the trend between PMs and $^*\text{CO}_2$ is opposite [Supplementary Figure 9A]. This means that for molecules with less PMs, $^*\text{CO}_2$ gains more charge, which is more conducive to the formation of C-H bonds activated by CO_2 plus H^+ , reducing the step energy barrier. The above results show that the Pb-N bonded small molecule passivator easily forms stronger IEF at the interface, which promotes better electron transport to the interface, thereby improving the photocatalytic performance of the structure.

In addition, Li *et al.* found that another important factor affecting photocatalysts is carrier kinetics, but this factor is directly related to effective mass, which refers to the ability of a carrier to transport light-excited carriers from the body to the surface^[65]. Therefore, the detailed study of these factors is of guiding significance for the rational design of perovskite photocatalysts. According to [Figure 9C](#) and [Supplementary Table 7](#), we find that the exciton E_b of the small molecule passivator with the Pb-N bond type at the interface is lower and the effective mass of the electrons is also reduced. The smaller effective mass helps enhance the diffusion rate of the charge carrier, which increases the rate of the photocatalytic reaction. Since the effective mass is determined by the secondary curvature of the CBM and valence band maximum (VBM), the larger the dispersion band, the smaller the effective mass. Compared with *d-p* orbital

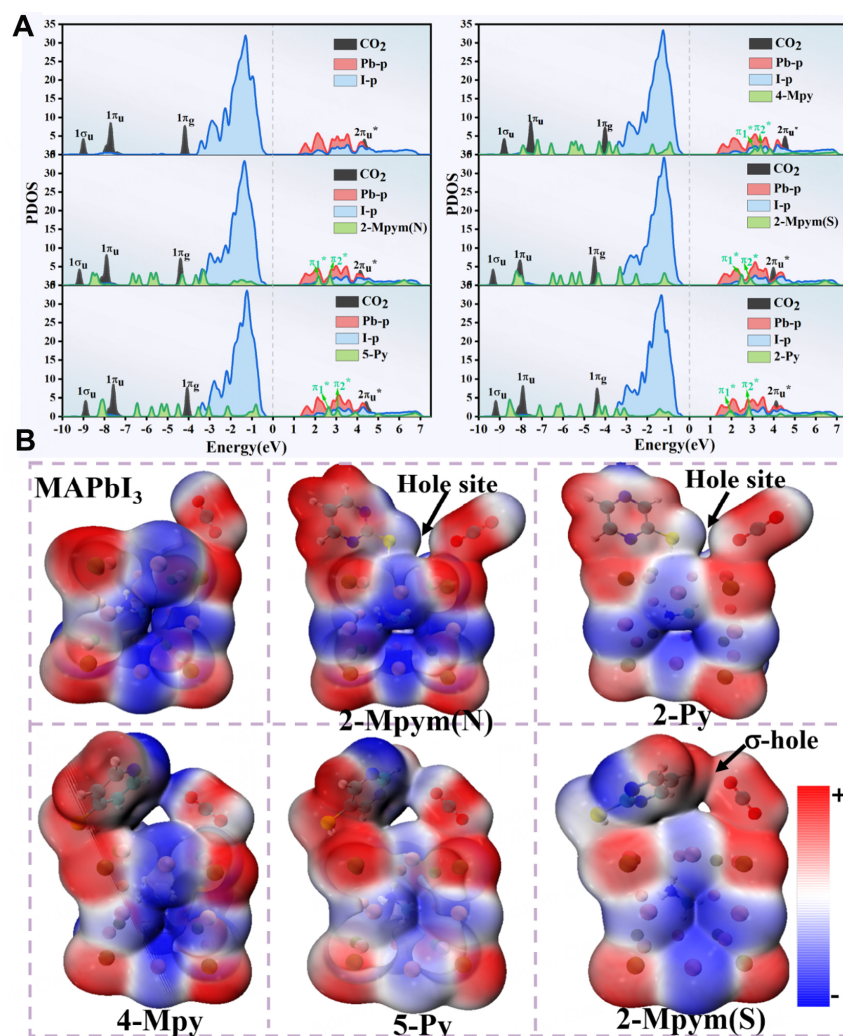


Figure 8. (A) Intrinsic structure and PMs@MAPbI₃ after CO₂ adsorption partial density of states (PDOS). Black font represents CO₂ orbital energy levels; green font represents LUMO orbital energy levels in PMs. (B) The electrostatic potential diagram of MAPbI₃ and PMs@MAPbI₃ adsorbed CO₂. Red indicates positivity, while blue indicates negativity.

hybridization, *s-p* orbital hybridization promotes more frequency band dispersion, reduces the effective mass, and increases the charge mobility, thereby improving the activity of the photocatalyst. The outermost orbitals of N and S are $2s^22p^3$ and $3s^23p^4$, respectively, and when they are coupled with the Pb $6s^26p^2$ orbital, the electrons in the *s* orbital of N are more involved in the coupling with the Pb $6p^2$ orbital. Combined with the free energy calculation, a complete heat map is provided [Figure 9D and Supplementary Tables 8-13]. The color indicates that the PMs@MAPbI₃ step data represents the overpotential, and it is easy to observe that the key step in forming Pb-N bond photocatalytic CO₂RR at the interface is the formation of *OCHOH, while the key step in Pb-S bond type CO₂RR is the desorption of *OCH₂. Therefore, the interaction strength between the intrinsic structure and Pb-N bond types *CO₂ and *OOCH determines the activity of the entire reaction. By using $E_{\text{COOH}}/E_{\text{CO}}$ as energy descriptors, as shown in Supplementary Figure 9B, a clear linear relationship exists between the adsorption energies of $E_{\text{CO}_2}/E_{\text{OOCH}_2}$; so, the energy barrier required for the next step can be determined by E_{CO_2} to predict the entire road strength and speed determination step.

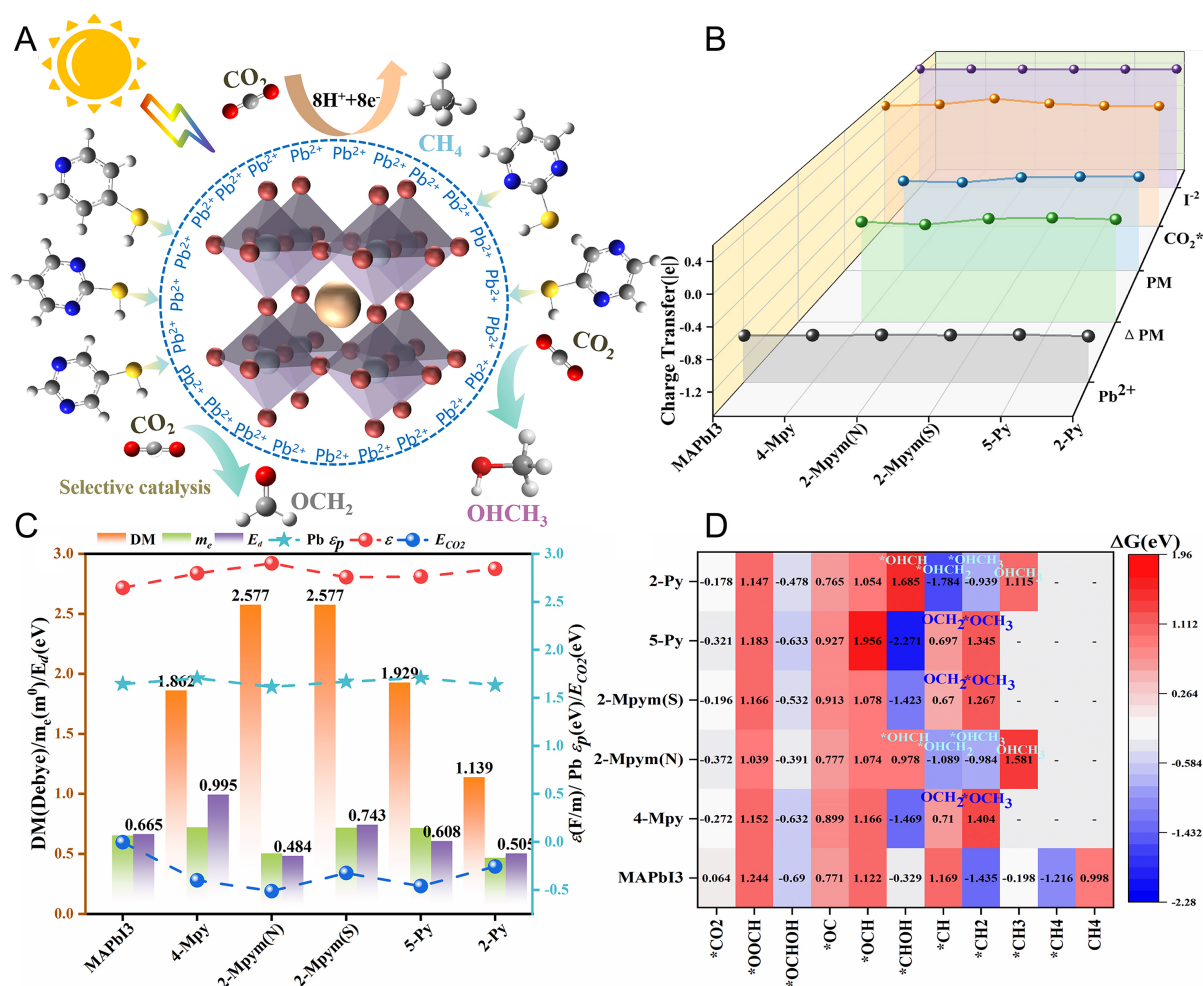


Figure 9. (A) Schematic diagram of selective catalysis. (B) After CO_2 adsorption at the interface, the comparison diagram of Bader charge transfer quantities for Pb^{2+} , I^{-2} , PMs, PMS, and $^*\text{CO}_2$ in the intrinsic structure and PMs@MAPbI₃. (C) The relationship diagram between various descriptors (such as dipole moment DM, electron effective mass m_e , exciton binding energy E_d , high-frequency dielectric constant ϵ , p -band center of Pb atoms ϵ_p , CO_2 adsorption energy E_{CO_2}). (D) Thermal potential diagrams of all activated states G during CO_2 reduction process.

Zuo et al. found that during photocatalytic CO_2 RR at the perovskite interface, protons are more likely to bond with C atoms to form $^*\text{OOCH}$ ^[45]. However, the adsorption of $^*\text{OOCH}$ is too weak, resulting in the catalytic step of $\text{CO}_2 \rightarrow ^*\text{OOCH}$ having to overcome a high energy barrier. It is important to note that $^*\text{OCHOH}$ desorption is an independent aprotic coupling [proton-coupled electron transfer (PCET)] step and is also a spontaneous process. Further dissociation into H_2O and $^*\text{CO}$ requires a high energy barrier, which is the determining step of the intrinsic structure. In addition, $^*\text{OCHOH} \rightarrow ^*\text{OC} + \text{H}_2\text{O}$ is a process that transitions from physical to chemical adsorption, which then reverts to physical adsorption in the subsequent PCET process to form $^*\text{OCH}$, as shown in Supplementary Figures 10 and 11. When the intermediate $^*\text{OCH}$ is converted to the next stage product, the products adsorbed by different PMs will change significantly. The intrinsic structure will form $^*\text{CHOH}$ and sit between the Pb-I bonds, and the C atom will twist downwards and adsorb onto the Pb atom, facilitating the breaking of the C-O bond and the formation of $^*\text{CH}$ in the subsequent chain reaction, ultimately preparing for the formation of $^*\text{CH}_4$. The structure with PMs makes the Pb-O bond stronger, promoting the conversion of CO_2 into alcohols and aldehydes by the substrate. When PMs form a Pb-S bond with the interface, protons are more likely to

adsorb onto C atoms in $^*\text{OCH}$ to form $^*\text{OCH}_2$ with a lower potential barrier, and the dissociation of $^*\text{OCH}_2$ is much smaller than the energy barrier for further H^+ addition. Therefore, the Pb-S bond promotes the ability of the interface to selectively convert CO_2 to CH_2O , but the energy barrier required for this process is higher than that for converting the intrinsic structure to CH_4 . When PMs form a Pb-N bond with the interface, H^+ is more easily adsorbed on the O atom in $^*\text{OCH}$ to form $^*\text{OHCH}$ (path 1 in Figure 10), which further forms $^*\text{OHCH}_2$ and promotes the formation of $^*\text{CH}_3\text{OH}$ in the structure. The potential barrier of the whole process is smaller than the intrinsic system, so the Pb-N bond can optimize the interface and selectively convert CO_2 to $^*\text{CH}_3\text{OH}$. Although the same PMs act differently on the interface, they can change the built-in charge distribution at the interface, promote changes in interface performance, and selectively generate alcohols, aldehydes, and other high carbon-based hydrogen compounds.

Catalytic performance of small molecule passivators themselves

Many studies have reported that the synergistic effect of organic molecules (such as Py and pyrimidine) adsorbed on metal electrodes can promote the selective electrocatalytic reduction of CO_2 and reduce the active barrier, enhancing the formation of carbon-based compounds^[66-68]. Zhang *et al.* even reported that fullerene C_{60} can act as an efficient and stable photocatalyst for halide perovskite nanocrystals to drive the reduction of CO_2 to CH_4 and CO ^[27]. This is because C_{60} , with its highly delocalized π bond structure, can act as an electron acceptor to obtain photogenerated electrons, thereby promoting charge separation and greatly improving the photocatalytic performance of the structure. From this perspective, we propose a bold hypothesis that the studied small molecule passivator can not only passivate perovskites, but also drive CO_2 for photoreduction. The autocatalytic mechanism of small organic molecules is shown in Figure 11A. In this process, CO and COOH can be generated, which reflects the cooperative transfer of proton electrons [sequential proton-electron transfer (SPET)].

The catalytic pathway of PMs studied in this article is shown in Figure 11B and C, Supplementary Figure 12. We found that the number of electrons from PMs to PMsH^+ increased from 6 to 7, leading to a spin effect (as shown in Supplementary Figure 13) that resulted in the loss of aromaticity and an increase in reduction potential. When CO_2 is driven by the interface, the N atom in PMsH attacks the C atom in CO_2 nucleophilically, transfers electrons to CO_2 for reduction, and at the same time restores the aromaticity of PMsH isomers, promotes proton transfer to form PMsCOOH , and reduces its energy barrier, as shown in Figure 11B. Supplementary Table 14 provides the specific values. In the following reaction, the N-C bond may also break to form COOH (type B), and the C-OH bond may break to form CO (type A). Both possibilities were investigated and it was found that 4-Mpy and 2-Mpym(N) were more inclined to selectively reduce CO_2 to formic acid. The energy barrier of 5-Py to generate COOH is too large, and the product is CO. Both 2-Py products have the potential to be generated. In summary, PMs act as catalysts at the interface, and the reaction is always endothermic. In reality, photocatalytic reduction of CO_2 is difficult to achieve, but the electrocatalytic reduction of CO_2 to COOH or CO on PMs with MAPbI_3 as the catalytic additive has a good application prospect.

CONCLUSION

We predicted the interfacial passivation performance of 2-Mpym and its analog passivator molecules by machine learning and verified them by DFT calculations. Supplementary Table 15 gives detailed definitions of the 26 eigenvectors used in ML. The results show that the chemical bonds formed by PMs at the interface can change the interfacial orbit characteristics, so that the results of interfacial passivation are different. For example, when PMs exhibit N-Pb and H-I chemical bonds with the interface, the interface stability can be enhanced. The transfer of electrons from PMs to the surface creates a strong built-in electric field at the interface, reducing charge accumulation at the interface and improving the PCE of the device. However, the

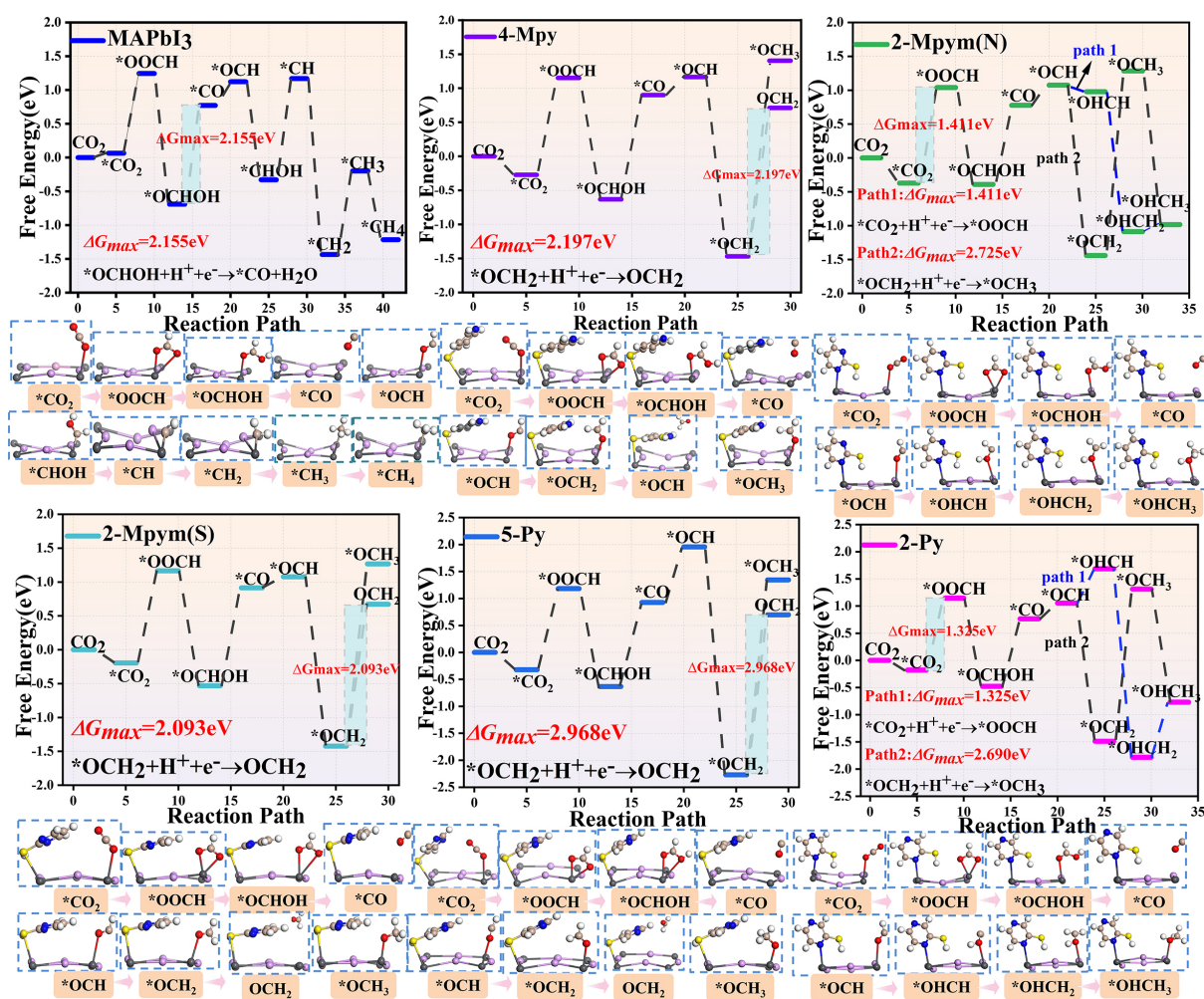


Figure 10. The intrinsic structure converts CO₂ to CH₄; 4-Mpy, 2-Mpym(S), and 5-Py converts CO₂ to CH₂O and 2-Mpym(N), and 2-Py converts CO₂ to CH₃OH in the free energy diagram.

formation of S-Pb ionic bonds at the interface of PMs leads to the deformation of the octahedral structure, resulting in the mismatch of the interface energy level and the decrease of the PCE of the device.

In the same PMs, different functional groups and interfacial bonding cause varying degrees of collapse of interfacial quantum effects. Based on this, we continue to explore the effect of PMs on the performance of interfacial photocatalytic CO₂RR. We found that the action of PMs on the perovskite interface would change the reduction path of CO₂ reduced by the original structured light, and at the same time, the interface would regularly promote the selective reduction of CO₂ to oxygenated carbon-based products. It can selectively reduce CO₂ to CH₃OH when the N-Pb bond is present on the interface. This is attributed to the interaction between the interface N-Pb bond and the SH... I coordinate bonds, which work synergistically to make the interface structure more stable. The O atom in CO₂ does not easily react with the functional group of PMs, resulting in the formation of larger hole points in the O and S at the bottom. When PMs form an S-Pb bond with the interface, CO₂ is selectively reduced to CH₂O. This is based on the fact that there is a lone pair of electrons between N and O atoms, which makes it easy to form polarized covalent bonds, which promotes CO₂ adsorption closer to PMs, resulting in *sp*² hybridization of carbon atoms and enhancing the adsorption of O atoms at the interface. After adsorption of CO₂ at the 2-Mpym(S)

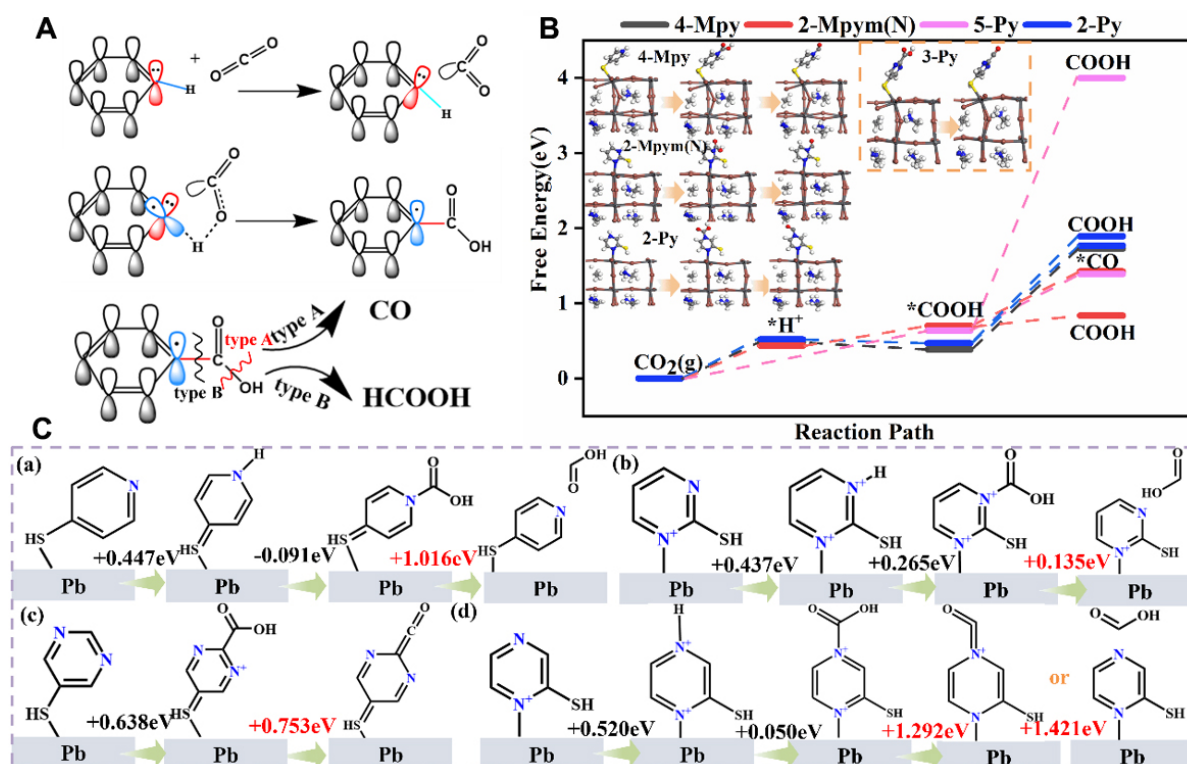


Figure 11. (A) Mechanism of CO₂ reduction catalyzed by organic molecules. (B) Free energy diagram of MAPbI₃ interface passivation for reducing CO₂ with different PMs. (C) Path diagrams of CO₂ reduction by different PMs. (a) is 4-Mpy; (b) is 2-Mpym(N); (c) is 5-Py; (d) is 2-Py. The black font represents the G energy required for the restoration path, and the red font represents the energy of G_{max} throughout the entire path.

interface, the head C-H bond gains electrons from O to form a non-covalent σ -hole bond, thereby reducing the catalytic reaction pathway. Finally, we explored the process of electron-coupled proton transfer of PMs acting on perovskites to reduce CO₂, and found that the loss of aromaticity of the molecular structure during the reaction process makes the reaction process require a large potential barrier, which is difficult to achieve in photoreduction. However, we speculate that electroreduction may be possible by using PMs as an additive in MAPbI₃, allowing CO₂ to be reduced to COOH or CO.

In this study, we propose a new method for designing passivators for organic-inorganic hybrid perovskite interfaces, and reveal the theoretical mechanism and influencing factors of passivators (PMs) for the selective reduction of CO₂ at the perovskite interface during photocatalysis. These findings provide theoretical guidance for PMs to improve CO₂ selectivity in perovskite interface photocatalysis. Looking ahead, we anticipate the practical application of selective photoreduction technology for PMs acting on perovskites in the experimental field. Future research could further explore the optimization of the bonding mode between the passivator and the interface by adjusting the chemical structure and functional groups of the passivator to improve the stability and selectivity of the photocatalyst. Ultimately, our goal is to achieve large-scale production and practical application, and promote the development of efficient and green energy conversion technologies.

DECLARATIONS

Authors' contributions

Conception and writing of the entire manuscript: Cai, Y.

Mentors and project leaders involved in the manuscript: Chen, C.
Participate in machine learning data analysis and guidance: Wang, Z.
Participate in data curation: Bai, Z.; Wang, S.; Zhang, Z.
Participate in methodology: Sun, M.; Xie, J.
Participate in validation and supervision: Li, D.; Guan, X.; Liu, G.
Provide resources and project support: Lu, P.; Yun, S.

Availability of data and materials

The data supporting the findings of this study are available within this Article and its [Supplementary Material](#). Further data are available from the corresponding authors upon request.

Financial support and sponsorship

This work was supported by the National Key Research and Development Program Projects of China (No. 2022YFB3204201), National Natural Science Foundation of China (Nos. 62305261, 62305262), Natural Science Foundation of Shaanxi Province (Nos. 2024JC-YBMS-021, 2024JC-YBMS-788, 2023-JC-YB-065), University Service Enterprise Project of Xi'an Science and Technology Bureau (No. 23GXFW0043), Cross-disciplinary Research and Cultivation Project of Xi'an University of Architecture and Technology (No. 2023JCPY-17), and the Xi'an University of Architecture and Technology Branch of Xi'an Computing Center.

Conflicts of interest

Yun, S. is an Editorial Board Member of the journal *Energy Materials*, while the other authors have declared that they have no conflicts of interest.

Ethical approval and consent to participate

Not applicable.

Consent for publication

Not applicable.

Copyright

© The Author(s) 2025.

REFERENCES

1. Liang, C.; Huang, Z.; Su, J.; Shi, L.; Liang, S.; Dong, Y. Study on performance optimization of perovskite solar cells based on MAPbI₃. *Adv. Theory. Simul.* **2024**, 7, 2301015. [DOI](#)
2. Stranks, S. D.; Eperon, G. E.; Grancini, G.; et al. Electron-hole diffusion lengths exceeding 1 micrometer in an organometal trihalide perovskite absorber. *Science* **2013**, 342, 341-4. [DOI](#)
3. Steirer, K. X.; Schulz, P.; Teeter, G.; et al. Defect tolerance in methylammonium lead triiodide perovskite. *ACS. Energy. Lett.* **2016**, 1, 360-6. [DOI](#)
4. Saouma, F. O.; Park, D. Y.; Kim, S. H.; Jeong, M. S.; Jang, J. I. Multiphoton absorption coefficients of organic-inorganic lead halide perovskites CH₃NH₃PbX₃ (X = Cl, Br, I) single crystals. *Chem. Mater.* **2017**, 29, 6876-82. [DOI](#)
5. Dobrovolsky, A.; Merdasa, A.; Li, J.; Hirslandt, K.; Unger, E. L.; Scheblykin, I. G. Relating defect luminescence and nonradiative charge recombination in MAPbI₃ perovskite films. *J. Phys. Chem. Lett.* **2020**, 11, 1714-20. [DOI](#) [PubMed](#)
6. Bi, Y.; Hutter, E. M.; Fang, Y.; Dong, Q.; Huang, J.; Savenije, T. J. Charge carrier lifetimes exceeding 15 μs in methylammonium lead iodide single crystals. *J. Phys. Chem. Lett.* **2016**, 7, 923-8. [DOI](#)
7. Wang, Q.; Niu, X.; Ning, W.; Zhu, Z.; Shi, R.; Zhao, Y. Interaction of organic-inorganic hybrid perovskite electron system with lattice system. *Mater. Today. Sustain.* **2024**, 25, 100617. [DOI](#)
8. Asuo, I. M.; Gedamu, D.; Ka, I.; et al. High-performance pseudo-halide perovskite nanowire networks for stable and fast-response photodetector. *Nano. Energy.* **2018**, 51, 324-32. [DOI](#)
9. Lian, X.; Wang, X.; Ling, Y.; et al. Light emitting diodes based on inorganic composite halide perovskites. *Adv. Funct. Mater.* **2019**,

- 29, 1807345. DOI
10. Qiu, L.; Ono, L. K.; Qi, Y. Advances and challenges to the commercialization of organic-inorganic halide perovskite solar cell technology. *Mater. Today. Energy*. **2018**, 7, 169-89. DOI
 11. Ma, Z.; Yuan, S.; Deng, J.; et al. Small-molecule targeting of defect passivation in all-inorganic carbon-based perovskite solar cells. *Solar. RRL*. **2023**, 7, 2201079. DOI
 12. Chen, C.; Cai, Y.; Zhang, Y.; et al. Exploring the effect of $C_6H_{5-x}F_xBr$ ($x=0-3$) passivating agent on surface properties at different termination ends: first principles. *Phys. Chem. Chem. Phys.* **2023**, 25, 29924-39. DOI
 13. Kan, C.; Hang, P.; Wang, S.; et al. Efficient and stable perovskite-silicon tandem solar cells with copper thiocyanate-embedded perovskite on textured silicon. *Nat. Photon.* **2025**, 19, 63-70. DOI
 14. Zhou, Q.; Gao, Y.; Cai, C.; et al. Dually-passivated perovskite solar cells with reduced voltage loss and increased super oxide resistance. *Angew. Chem. Int. Ed.* **2021**, 60, 8303-12. DOI
 15. Wei, J.; Wang, Q.; Huo, J.; et al. Mechanisms and suppression of photoinduced degradation in perovskite solar cells. *Adv. Energy. Mater.* **2021**, 11, 2002326. DOI
 16. Oner, S. M.; Sezen, E.; Yordanli, M. S.; Karakoc, E.; Deger, C.; Yavuz, I. Surface defect formation and passivation in formamidinium lead triiodide (FAPbI₃) perovskite solar cell absorbers. *J. Phys. Chem. Lett.* **2022**, 13, 324-30. DOI PubMed
 17. Lin, C.; Li, S.; Zhang, W.; Shao, C.; Yang, Z. Effect of bromine substitution on the ion migration and optical absorption in MAPbI₃ perovskite solar cells: the first-principles study. *ACS. Appl. Energy. Mater.* **2018**, 1, 1374-80. DOI
 18. Feng, X.; Liu, B.; Peng, Y.; et al. Restricting the formation of Pb-Pb dimer via surface Pb site passivation for enhancing the light stability of perovskite. *Small* **2022**, 18, e2201831. DOI
 19. Wang, S.; Wang, A.; Deng, X.; et al. Lewis acid/base approach for efficacious defect passivation in perovskite solar cells. *J. Mater. Chem. A*. **2020**, 8, 12201-25. DOI
 20. Wang, Z.; Pradhan, A.; Kamarudin, M. A.; et al. Passivation of grain boundary by squaraine zwitterions for defect passivation and efficient perovskite solar cells. *ACS. Appl. Mater. Interfaces*. **2019**, 11, 10012-20. DOI
 21. Senftle, T. P.; Lessio, M.; Carter, E. A. The role of surface-bound dihydropyridine analogues in pyridine-catalyzed CO₂ reduction over semiconductor photoelectrodes. *ACS. Cent. Sci.* **2017**, 3, 968-74. DOI PubMed PMC
 22. Senftle, T. P.; Lessio, M.; Carter, E. A. Interaction of pyridine and water with the reconstructed surfaces of GaP(111) and CdTe(111) photoelectrodes: implications for CO₂ reduction. *Chem. Mater.* **2016**, 28, 5799-810. DOI
 23. Yuan, J.; Zheng, L.; Hao, C. Role of pyridine in photoelectrochemical reduction of CO₂ to methanol at a CuInS₂ thin film electrode. *RSC. Adv.* **2014**, 4, 39435-8. DOI
 24. Jeon, J. H.; Mareeswaran, P. M.; Choi, C. H.; Woo, S. I. Synergism between CdTe semiconductor and pyridine - photoenhanced electrocatalysis for CO₂ reduction to formic acid. *RSC. Adv.* **2014**, 4, 3016-9. DOI
 25. Lim, C. H.; Holder, A. M.; Hynes, J. T.; Musgrave, C. B. Reduction of CO₂ to methanol catalyzed by a biomimetic organo-hydride produced from pyridine. *J. Am. Chem. Soc.* **2014**, 136, 16081-95. DOI PubMed
 26. Pan, Y.; Liu, X.; Zhang, W.; et al. Advances in photocatalysis based on fullerene C60 and its derivatives: properties, mechanism, synthesis, and applications. *Appl. Catal. B. Environ.* **2020**, 265, 118579. DOI
 27. Zhang, Z.; Shu, M.; Jiang, Y.; Xu, J. Fullerene modified CsPbBr₃ perovskite nanocrystals for efficient charge separation and photocatalytic CO₂ reduction. *Chem. Eng. J.* **2021**, 414, 128889. DOI
 28. Hameed, T. A.; Mohamed, F.; Abd-El-Messieh, S. L.; Ward, A. Methylammonium lead iodide/poly(methyl methacrylate) nanocomposite films for photocatalytic applications. *Mater. Chem. Phys.* **2023**, 293, 126811. DOI
 29. Wu, Z.; Bi, E.; Ono, L. K.; et al. Passivation strategies for enhancing device performance of perovskite solar cells. *Nano. Energy*. **2023**, 115, 108731. DOI
 30. Zhi, C.; Wang, S.; Sun, S.; et al. Machine-learning-assisted screening of interface passivation materials for perovskite solar cells. *ACS. Energy. Lett.* **2023**, 8, 1424-33. DOI
 31. Mai, Y.; Tang, J.; Meng, H.; et al. Machine learning-based screening of two-dimensional perovskite organic spacers. *Adv. Compos. Hybrid. Mater.* **2024**, 7, 910. DOI
 32. Wu, Z.; Kang, L.; Huang, T.; et al. Elevating perovskite efficiency via machine learning-assisted screening of passivators. *Chem. Eng. J.* **2024**, 499, 156391. DOI
 33. Wang, D.; Thunell, S.; Lindberg, U.; Jiang, L.; Trygg, J.; Tysklind, M. Towards better process management in wastewater treatment plants: process analytics based on SHAP values for tree-based machine learning methods. *J. Environ. Manag.* **2022**, 301, 113941. DOI
 34. Zhang, X.; Ding, B.; Wang, Y.; et al. Machine learning for screening small molecules as passivation materials for enhanced perovskite solar cells. *Adv. Funct. Mater.* **2024**, 34, 2314529. DOI
 35. Liu, Y.; Wang, Y.; Zhang, J. New machine learning algorithm: random forest. In: Liu, B.; Ma, M.; Chang, J. editors. Information computing and applications. Berlin: Springer; 2012. pp. 246-52. DOI
 36. Noble, W. S. What is a support vector machine? *Nat. Biotechnol.* **2006**, 24, 1565-7. DOI PubMed
 37. Kramer, O. Dimensionality reduction with unsupervised nearest neighbors. Springer; 2013. Available from: <https://link.springer.com/book/10.1007/978-3-642-38652-7> [Last accessed on 6 Feb 2025]
 38. Natekin, A.; Knoll, A. Gradient boosting machines, a tutorial. *Front. Neurobot.* **2013**, 7, 21. DOI PubMed PMC
 39. Kresse, G.; Furthmüller, J. Efficiency of ab-initio total energy calculations for metals and semiconductors using a plane-wave basis set.

- Comput. Mater. Sci.* **1996**, *6*, 15-50. DOI
40. Tang, T.; Tang, Y. A first principle comparison of arsenic-based double halide perovskite materials for photovoltaic and optoelectronic application. *J. Solid. State. Chem.* **2022**, *316*, 123557. DOI
41. Mwankemwa, N.; Wang, H.; Zhu, T.; Fan, Q.; Zhang, F.; Zhang, W. First principles calculations investigation of optoelectronic properties and photocatalytic CO₂ reduction of (MoSi₂N₄)_{5-n}/(MoSiGeN₄)_n in-plane heterostructures. *Results. Phys.* **2022**, *37*, 105549. DOI
42. Cai, Y.; Chen, C.; Chen, F.; et al. Theoretical exploration of CO₂ photocatalytic reduction using single atom gold nanoparticles (Au⁰) modified SrTi_{0.875}Hf_{0.125}O₃. *J. Catal.* **2024**, *432*, 115410. DOI
43. Wang, F.; Xie, W.; Yang, L.; Xie, D.; Lin, S. Revealing the importance of kinetics in N-coordinated dual-metal sites catalyzed oxygen reduction reaction. *J. Catal.* **2021**, *396*, 215-23. DOI
44. Guo, M.; Ji, M.; Cui, W. Theoretical investigation of HER/OER/ORR catalytic activity of single atom-decorated graphyne by DFT and comparative DOS analyses. *App. Surf. Sci.* **2022**, *592*, 153237. DOI
45. Zuo, X.; Chang, K.; Zhao, J.; et al. Bubble-template-assisted synthesis of hollow fullerene-like MoS₂ nanocages as a lithium ion battery anode material. *J. Mater. Chem. A* **2016**, *4*, 51-8. DOI
46. Tripathi, A.; Thapa, R. Optimizing CO₂RR selectivity on single atom catalysts using graphical construction and identification of energy descriptor. *Carbon* **2023**, *208*, 330-7. DOI
47. Son, C.; Son, H.; Jeong, B. Enhanced conversion efficiency in MAPbI₃ perovskite solar cells through parameters optimization via SCAPS-1D simulation. *Appl. Sci.* **2024**, *14*, 2390. DOI
48. Morales-Acevedo, A.; Hernández-Como, N.; Casados-Cruz, G. Modeling solar cells: a method for improving their efficiency. *Mater. Sci. Eng. B* **2012**, *177*, 1430-5. DOI
49. Burgelman, M.; Verschraegen, J.; Degraeve, S.; Nollet, P. Modeling thin-film PV devices. *Prog. Photovoltaics* **2004**, *12*, 143-53. DOI
50. Benesty, J.; Chen, J.; Huang, Y.; Cohen, I. Pearson correlation coefficient. In: noise reduction in speech processing. Berlin: Springer; 2009. pp. 1-4. DOI
51. Novaković, J. D.; Veljović, A.; Ilić, S. S.; Papić, Ž.; Tomović, M. Evaluation of classification models in machine learning. *Theory. Appl. Math. Comput. Sci.* **2017**, *7*, 39-46. Available from: <https://www.proquest.com/docview/1922445698?sourcetype=Scholarly%20Journals> [Last accessed on 6 Feb 2025]
52. Zang, J.; Zhang, C.; Qiang, Y.; Liu, Q.; Fei, Y.; Yu, Z. Efficient and stable planar MAPbI₃ perovskite solar cells based on a small molecule passivator. *Surf. Interfaces* **2021**, *25*, 101213. DOI
53. Ma, X.; Li, Z. The effect of oxygen molecule adsorption on lead iodide perovskite surface by first-principles calculation. *Appl. Surf. Sci.* **2018**, *428*, 140-7. DOI
54. Filip, M. R.; Verdi, C.; Giustino, F. *GW* band structures and carrier effective masses of CH₃NH₃PbI₃ and hypothetical perovskites of the type APbI₃: A = NH₄, PH₄, AsH₄, and SbH₄. *J. Phys. Chem. C* **2015**, *119*, 25209-19. DOI
55. Zhao, L.; Grande-Aztatzi, R.; Foroutan-Nejad, C.; Ugalde, J. M.; Frenking, G. Aromaticity, the Hückel 4n+2 rule and magnetic current. *ChemistrySelect* **2017**, *2*, 863-70. DOI
56. Zhao, Z.; Lu, G. Circumventing the scaling relationship on bimetallic monolayer electrocatalysts for selective CO₂ reduction. *Chem. Sci.* **2022**, *13*, 3880-7. DOI PubMed PMC
57. Chen, X.; Xu, Y.; Ma, X.; Zhu, Y. Large dipole moment induced efficient bismuth chromate photocatalysts for wide-spectrum driven water oxidation and complete mineralization of pollutants. *Natl. Sci. Rev.* **2020**, *7*, 652-9. DOI PubMed PMC
58. Wang, G.; Cheng, D.; He, T.; et al. Enhanced visible-light responsive photocatalytic activity of Bi₂₅FeO₄₀/Bi₂Fe₄O₉ composites and mechanism investigation. *J. Mater. Sci. Mater. Electron.* **2019**, *30*, 10923-33. DOI
59. Al-Shami, A.; Sibari, A.; Mansouri, Z.; et al. Photocatalytic properties of ZnO:Al/MAPbI₃/Fe₂O₃ heterostructure: first-principles calculations. *Int. J. Mol. Sci.* **2023**, *24*, 4856. DOI PubMed PMC
60. Hammer, B.; Norskov, J. K. Why gold is the noblest of all the metals. *Nature* **1995**, *376*, 238-40. DOI
61. Jacobs, R.; Hwang, J.; Shao-Horn, Y.; Morgan, D. Assessing correlations of perovskite catalytic performance with electronic structure descriptors. *Chem. Mater.* **2019**, *31*, 785-97. DOI
62. Wang, T.; Zhang, C.; Wang, J.; et al. The interplay between the suprafacial and intrafacial mechanisms for complete methane oxidation on substituted LaCoO₃ perovskite oxides. *J. Catal.* **2020**, *390*, 1-11. DOI
63. Xiang, D.; Magana, D.; Dyer, R. B. CO₂ reduction catalyzed by mercaptopteridine on glassy carbon. *J. Am. Chem. Soc.* **2014**, *136*, 14007-10. DOI
64. Zhou, W.; Jing, Q.; Li, J.; Chen, Y.; Hao, G.; Wang, L. Organic photocatalysts for solar water splitting: molecular- and aggregate-level modifications. *Acta. Phys. Chim. Sin.* **2023**, *9*, 2211010. DOI
65. Li, X.; Mai, H.; Lu, J.; et al. Rational atom substitution to obtain efficient, lead-free photocatalytic perovskites assisted by machine learning and DFT calculations. *Angew. Chem. Int. Ed.* **2023**, *62*, e202315002. DOI
66. Ashaduzzaman, M.; Kang, X.; Strange, L.; Pan, S. Electrocatalytic CO₂ reduction at pyridine functionalized Au nanoparticles supported by NanoCOT electrode. *J. Electrochem. Soc.* **2022**, *169*, 116510. DOI
67. Vasilyev, D. V.; Dyson, P. J. The role of organic promoters in the electroreduction of carbon dioxide. *ACS. Catal.* **2021**, *11*, 1392-405. DOI
68. Yu, M.; Doak, P.; Tamblyn, I.; Neaton, J. B. Theory of covalent adsorbate frontier orbital energies on functionalized light-absorbing semiconductor surfaces. *J. Phys. Chem. Lett.* **2013**, *4*, 1701-6. DOI PubMed